Supporting Information

Synergetic Enhancement of $CsPbI_3$ Nanorods-based High-Performance Photodetectors via PbSe Quantum Dot Interface Engineering

Muhammad Sulaman[1, 2], Shengyi Yang[1*], Honglian Guo[2], Chuanbo Li[2], Ali Imran[3], Arfan Bukhtiar[4], Muhammad Qasim[5], Zhenhua Ge[1], Yong Song[5], Yurong Jiang[5], Bingsuo Zou[4]

[1] Beijing Key Lab of Nanophotonics and Ultrafine Optoelectronic Systems, Center for Micro-Nanotechnology, School of Physics, Beijing Institute of Technology, Beijing 100081, P. R. China; Key Lab of Advanced Optoelectronic Quantum Design and Measurement, Ministry of Education, School of Physics, Beijing Institute of Technology, Beijing 100081, P. R. China.
[2] Optoelectronics Research Center, School of Science, Minzu University of China, Beijing, 100081, China

[3] School of Micro-Nanoelectronics, ZJU-Hangzhou Global Scientific and Technological Innovation Center, State Key Labs of Silicon Materials and Modern Optical Instrumentation, Zhejiang University, Hangzhou 311200, China.
[4] MOE Key Lab of New Processing Technology for Nonferrous Metals and Materials and Guangxi Key Lab of Processing for Nonferrous Metals and Featured Materials, School of Resources, Environments and Materials, Guangxi University, Nanning 530004, P. R. China.
[5] Beijing Key Lab for Precision Optoelectronic Measurement Instrument and Technology, School of Optics and Photonics, Beijing Institute of Technology, Beijing 100081, P. R. China.

Corresponding Author, E-mail: syyang@bit.edu.cn

Note S1. Synthesis of ZnO nanoparticles

ZnO nanoparticles were synthesized using a sol-gel method to ensure the production of high-quality nanocrystals. The synthesis procedure involved the preparation of two separate solutions. In the first solution, hydrated zinc acetate (3 mmol) was dissolved in 30 mL of methanol. The second solution consisted of potassium hydroxide (2 mmol) dissolved in 20 mL of methanol. Continuous magnetic stirring was applied throughout the process. The second solution was slowly injected into the first solution over a period of 10 minutes while maintaining continuous stirring. The reaction took place at a temperature of 60 °C with continuous stirring for 10 hours. Following the reaction, the crystalline ZnO nanoparticles were precipitated by adding ethyl acetate. The resulting precipitate was then re-dispersed into ethanol for further use and characterization.

Note S2. Synthesis of PbSe CQDs

In brief, two solutions were prepared following a specific procedure. In the first solution, PbO (4 mmol) was dissolved in a mixture of oleic acid (OA) (10 mmol) and 1-Octadecene (ODE) in a 3-necked flask. Continuous stirring was maintained at 40 °C throughout the process. To ensure an oxygen-free environment, the reaction vessel was purged with nitrogen gas three times, each time for 20 minutes. The temperature of the solution was gradually raised to 180 °C and held at this temperature for 1 hour. During this time, the solution's color transformed from colorless to light yellow, then to bright yellow, and finally to dark brown. The second solution, containing the selenium (Se) precursor, was prepared by dissolving Se in tri-n-octylphosphine (TOP) using ultrasonication for 2 hours until complete dissolution and a colorless solution was obtained. Upon completion of the Se solution, it was rapidly injected into the hot PbO/OA/ODE solution. The temperature was slightly reduced to 170 °C, and the reaction proceeded for 180 seconds. To stop the reaction, 5 mL of n-Hexane was quickly injected. To enhance the conductivity and stability of the quantum dots, a solution of NH4Cl in methyl alcohol was added to the reaction mixture and allowed to react for 10 minutes at 60 °C. After cooling the final solution to room temperature, the synthesized CQDs were purified by washing twice with a mixture of n-Hexane, isopropyl alcohol,

and ethanol, followed by a final wash with a mixture of n-Hexane, isopropyl alcohol, and acetone. The purified CQDs were then dried in a vacuum oven at 50 °C for 24 hours. The resulting CQDs were collected after drying and could be re-dispersed in different solvents to form a colloidal solution suitable for spin-coating or other applications.

Note S3. Equipment Specifications

With the aid of a UV-vis-NIR spectrophotometer (Shimadzu, UV-3600), the absorption spectra of the nanomaterials were examined. Using a semiconductor parameter analyzing system (Keithley 4200-SCS), electrical and optical properties of the devices were assessed both in the absence of light and under illumination by several laser wavelengths, including 405 nm, 532 nm, 980 nm, and 1550 nm. A ZEISS SUPRA-55 was used to take the field emission scanning electron microscopy (FESEM) pictures of the CQD films. A Jeol JEM-2100F was used to capture the high-resolution transmission electron microscopy (HR-TEM) pictures of the CQDs. The Philips X'Pert Pro MPD was used to record the x-ray diffraction (XRD) patterns. The PHI QUANTERA-II SXM spectrometer measured the X-ray photoelectron spectroscopy (XPS) spectrum and the ultraviolet photoelectron spectroscopy (UPS) data. Each characterization was carried out in ambient air at room temperature.

Note S4. Theoretical Simulation

TCAD Sentaurus (N-2017.06) played a pivotal role in our comprehensive investigation of the photoactive layers within organic-inorganic heterointerfaces and blended nanocomposites for diverse device simulations. In particular, the transport of carriers across the interface between PbSe and inorganic perovskite ($CsPbI_3$) was studied using the thermionic emission model. This model is grounded in a meticulous numeric analysis of electromagnetic waves and quasi-stationary simulations, providing valuable insights into carrier dynamics at this critical junction. Additionally, our study delved into the blended materials, maintaining a 1:1 ratio as defined by the thermionic emission model. This approach facilitated the creation of interfaces with the blended semiconductor, specifically $ZnO:Cs_2CO_3$, which is instrumental in our device structure.

Employing numerical analysis and the quasi-stationary method, we comprehensively examined the optical and electronic behaviors inherent in these devices. To unravel the optical generation and absorbed photon density, we harnessed the Electromagnetic Wave (EMW) Solver, a powerful tool based on the finite-difference time-domain (FDTD) method. This enabled precise calculations, shedding light on the intricate interplay of light absorption within the active layers. For modeling the electrical behavior within the organic components, we implemented Gaussian density of states (DOS) alongside the Poole Frankel Mobility model, which incorporates high-field saturation effects. Moreover, recombination processes were factored in, employing the singlet exciton model. This comprehensive framework allowed us to gain deeper insights into charge transport and mobility within the devices, particularly the square root dependence on the electric field, as elucidated by the Poole-Frankel Mobility model integrated with the High-Field Saturation model.

Through these multifaceted simulations, we advanced our understanding of the sophisticated workings of the devices, effectively bridging the gap between theory and experiment in our pursuit of high-performance photodetectors.

Details of computational aspects in conjunction with the experiments

TCAD Sentaurus (N-2017.06) was employed for comprehensive investigations of the photoactive layers within organic-inorganic heterointerfaces and blended nanocomposites. The simulations focused on understanding the transport of carriers across the interface between PbSe and inorganic perovskite ($CsPbI_3$). Specifically, the thermionic emission model was utilized, grounded in meticulous numeric analysis of electromagnetic waves and quasi-stationary simulations. This model provides valuable insights into carrier dynamics at the critical heterojunction.

The study delved into blended materials, maintaining a 1:1 ratio, as defined by the thermionic emission model. This approach facilitated the creation of interfaces with the blended semiconductor, specifically $ZnO:Cs_2CO_3$, a crucial element in our device structure. Through

numerical analysis and the quasi-stationary method, we comprehensively examined the optical and electronic behaviors inherent in these devices.

To unravel the optical generation and absorbed photon density, we harnessed the Electromagnetic Wave (EMW) Solver, a powerful tool based on the finite-difference time-domain (FDTD) method. This allowed precise calculations, shedding light on the intricate interplay of light absorption within the active layers. For modeling the electrical behavior within the organic components, we implemented Gaussian density of states (DOS) alongside the Poole Frankel Mobility model, which incorporates high-field saturation effects. Recombination processes were factored in, employing the singlet exciton model. This comprehensive framework enabled a deeper understanding of charge transport and mobility within the devices.

Theoretical simulations were crucial in aligning our computational results with experimental observations. By bridging the gap between theory and experiment, we gained a holistic understanding of the sophisticated workings of the devices. This alignment enhances the predictive power of our computational model, allowing us to optimize device performance based on theoretical insights. In summary, the computational aspects, specifically TCAD Sentaurus simulations, played a key role in supplementing experimental findings. By simulating the behavior of carriers, understanding optical generation, and modeling electrical characteristics, we achieved a comprehensive understanding of the $CsPbI_3$/PbSe heterojunction photodetector. This integration of computational and experimental approaches is instrumental in advancing the field of optoelectronic devices and lays the foundation for designing high-performance photodetectors.

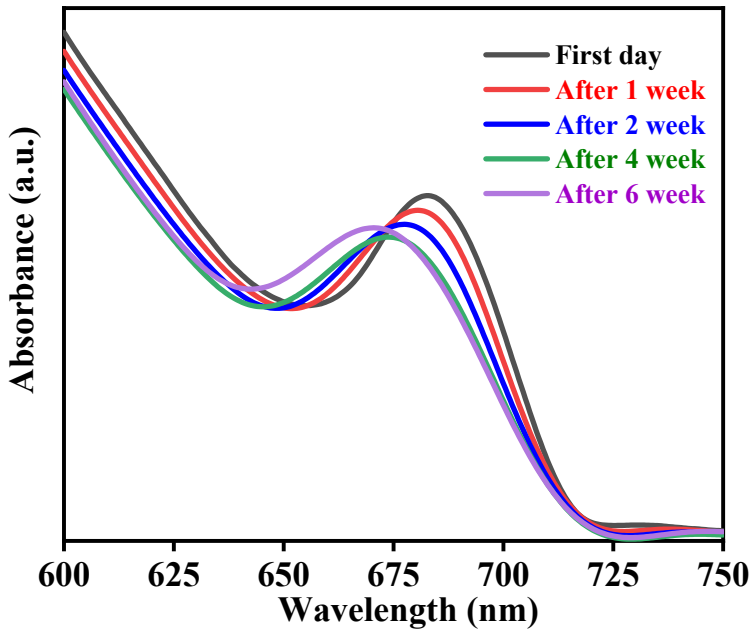

Figure S1. UV-Vis absorption spectra of $CsPbI_3$ after different intervals of time to confirm its stability.

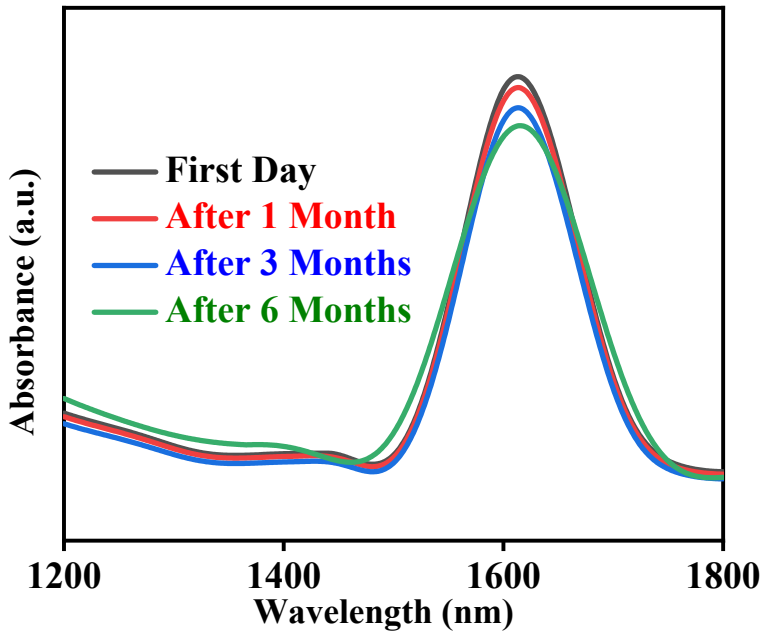

Figure S2. UV-Vis absorption spectra of PbSe after different intervals of time to confirm its stability.

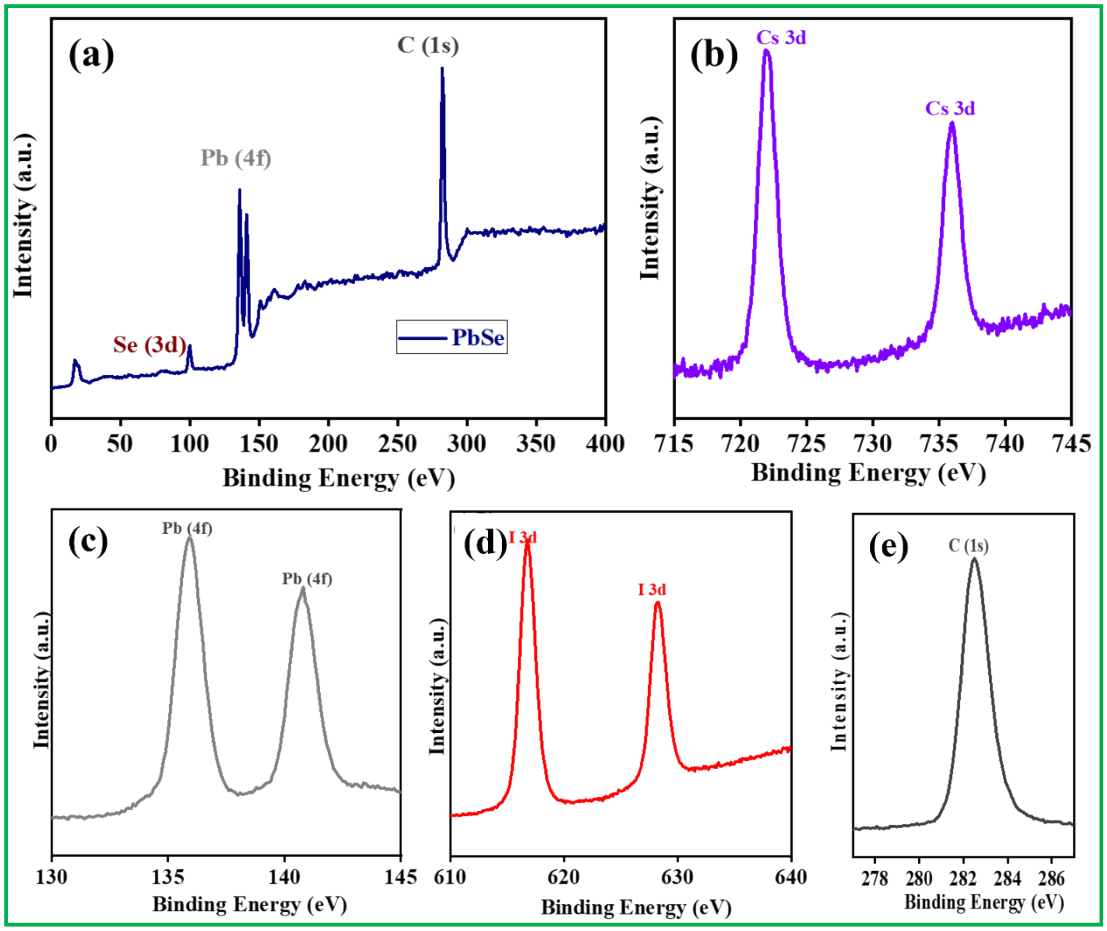

Figure S3. XPS spectra of all individual major components (Pb, Se, Cs, I and C) with their orbital orientations.

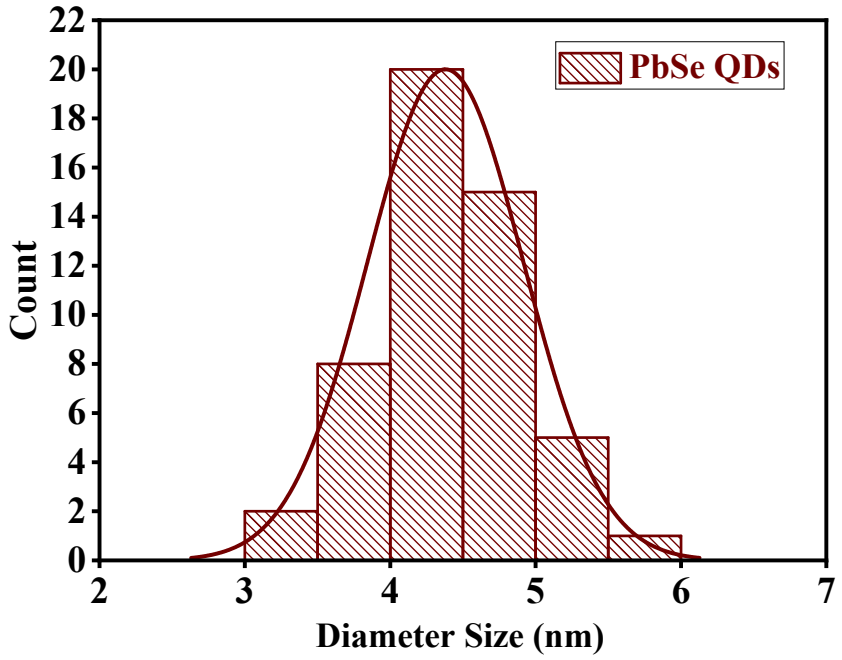

Figure S4. Size distribution plot of the PbSe QDs extracted from original TEM image to estimate the average diameter size of the particles.

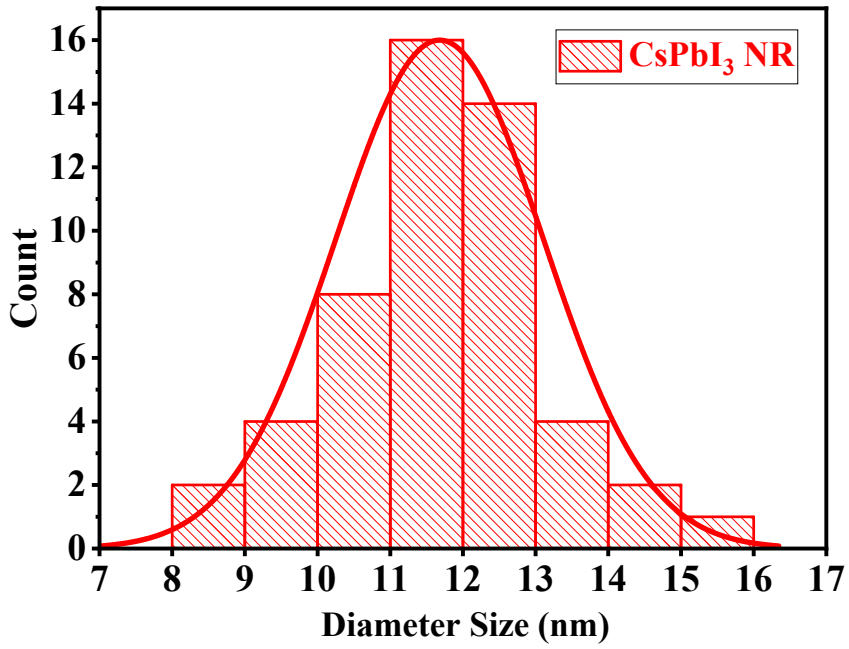

Figure S5. Size distribution plot of the $CsPbI_3$ NRs extracted from original TEM image to estimate the average diameter size of the NRs.

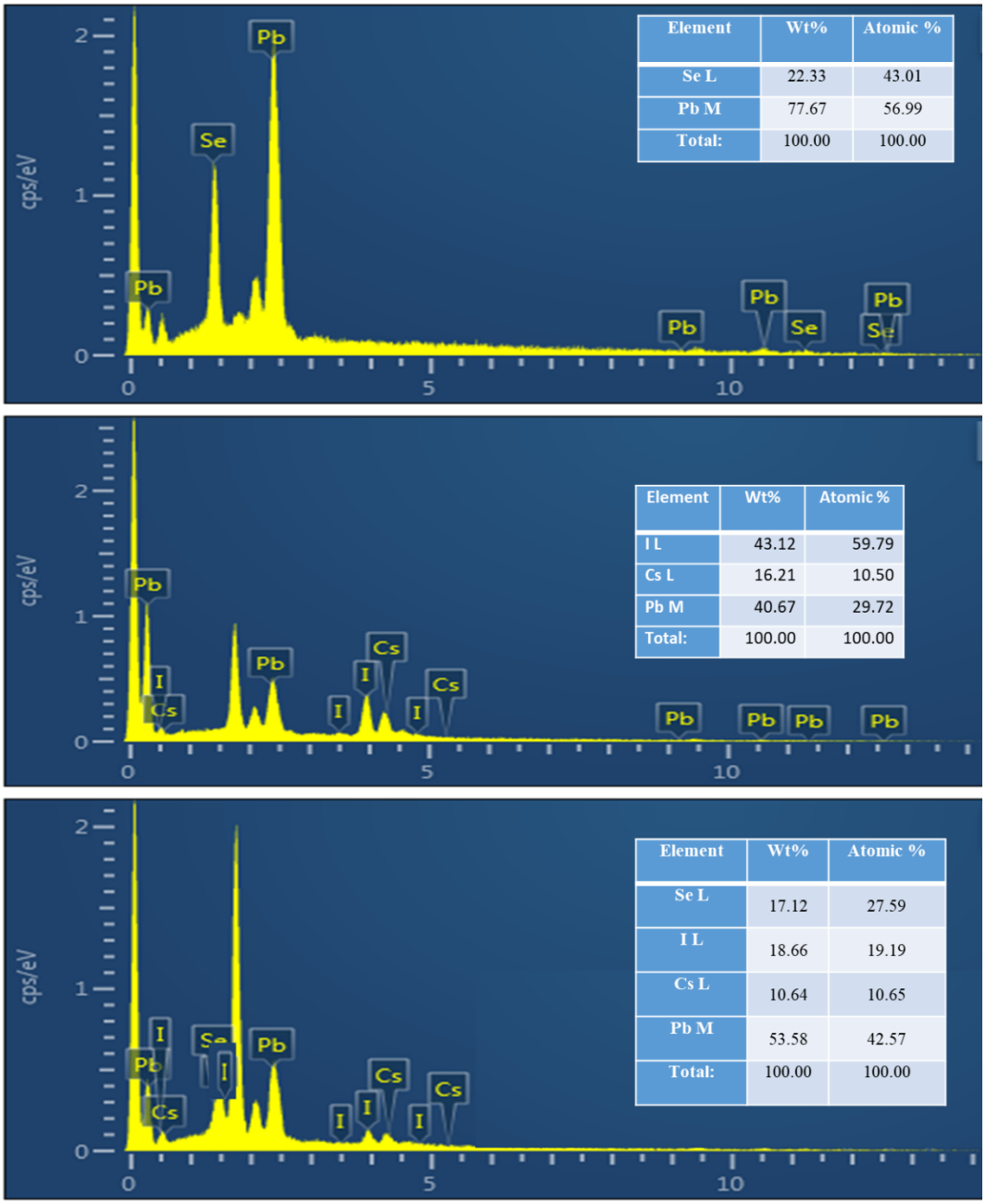

Figure S6. EDS spectra of pristine PbSe, $CsPbI_3$ and their hybrid nanocomposite presenting all the peaks of the major elements (Pb, Se, Cs, and I) with their weight and atomic percentages.

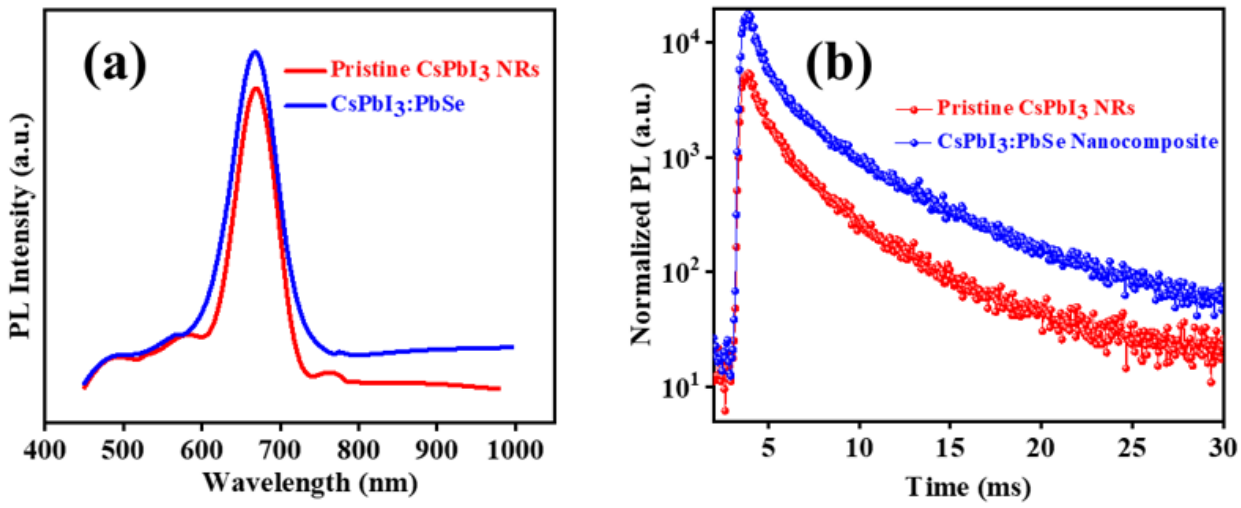

Figure S7. Photoluminescence (PL) intensity (**a**), and time-resolved PL (**b**) of pristine $CsPbI_3$ NRs and blended nanocomposite of $CsPbI_3$:PbSe.

Table S1: The parameters for $CsPbI_3$ and $CsPbI_3$:PbSe extracted from TRPL data.

Parameters	**CsPbI3**	**CsPbI3:PbSe**
A_1	2.47×10^6	1.13×10^6
A_2	10773.9	20317.27
τ_1	0.58317	0.5692
τ_2	2.50643	3.03371
τ_{ave}	5.74×10^{-1}	5.92×10^{-1}

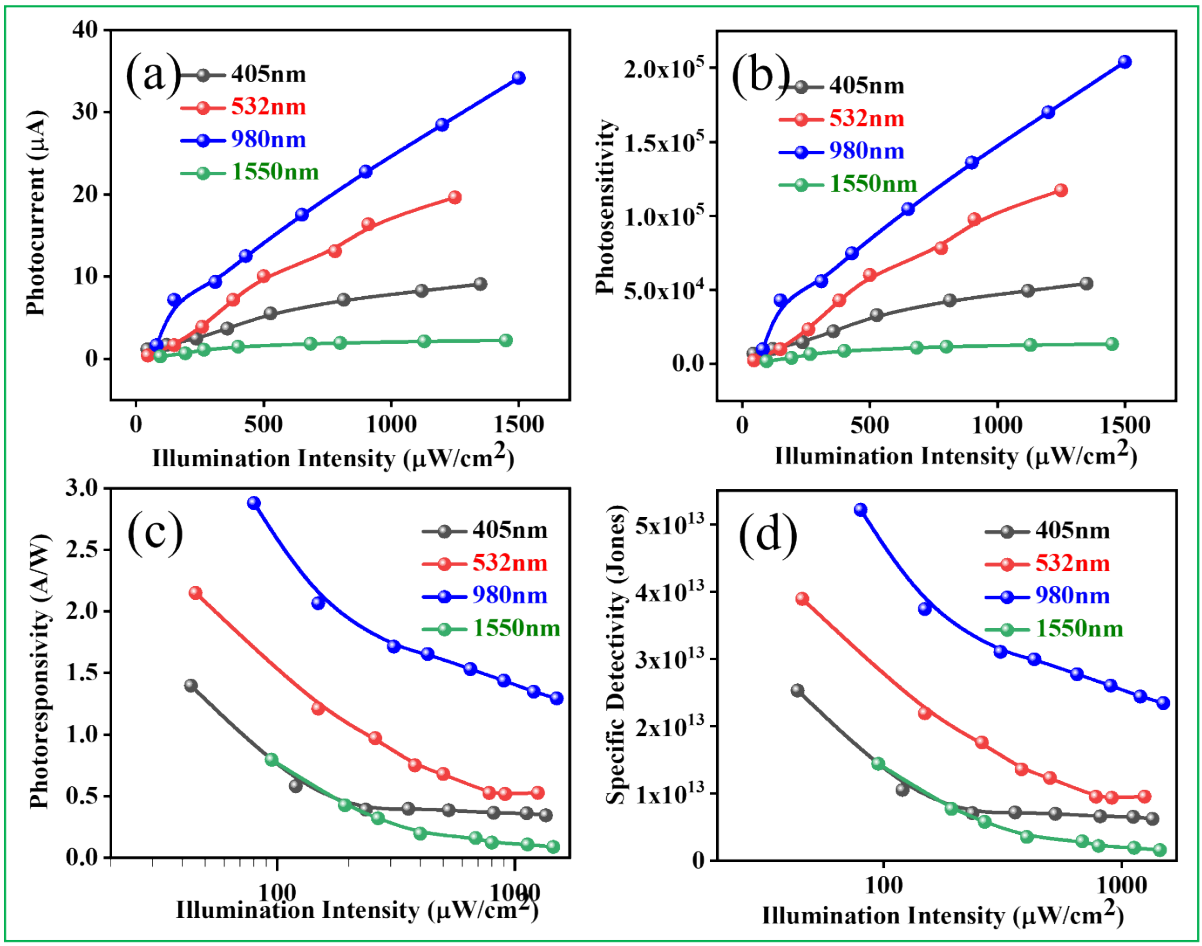

Figure S8. Performance of the photodetector ITO/ZnO/$CsPbI_3$/PbSe/CuSCN/P3HT/Au (device **A**). Photocurrent (**a**), photosensitivity (**b**), photoresponsivity (*R*) (**c**), and specific detectivity (D^*) (**d**) as functions of illumination intensity in self-driven mode under 405 nm, 532 nm, 980 nm, and 1550 nm illuminations.

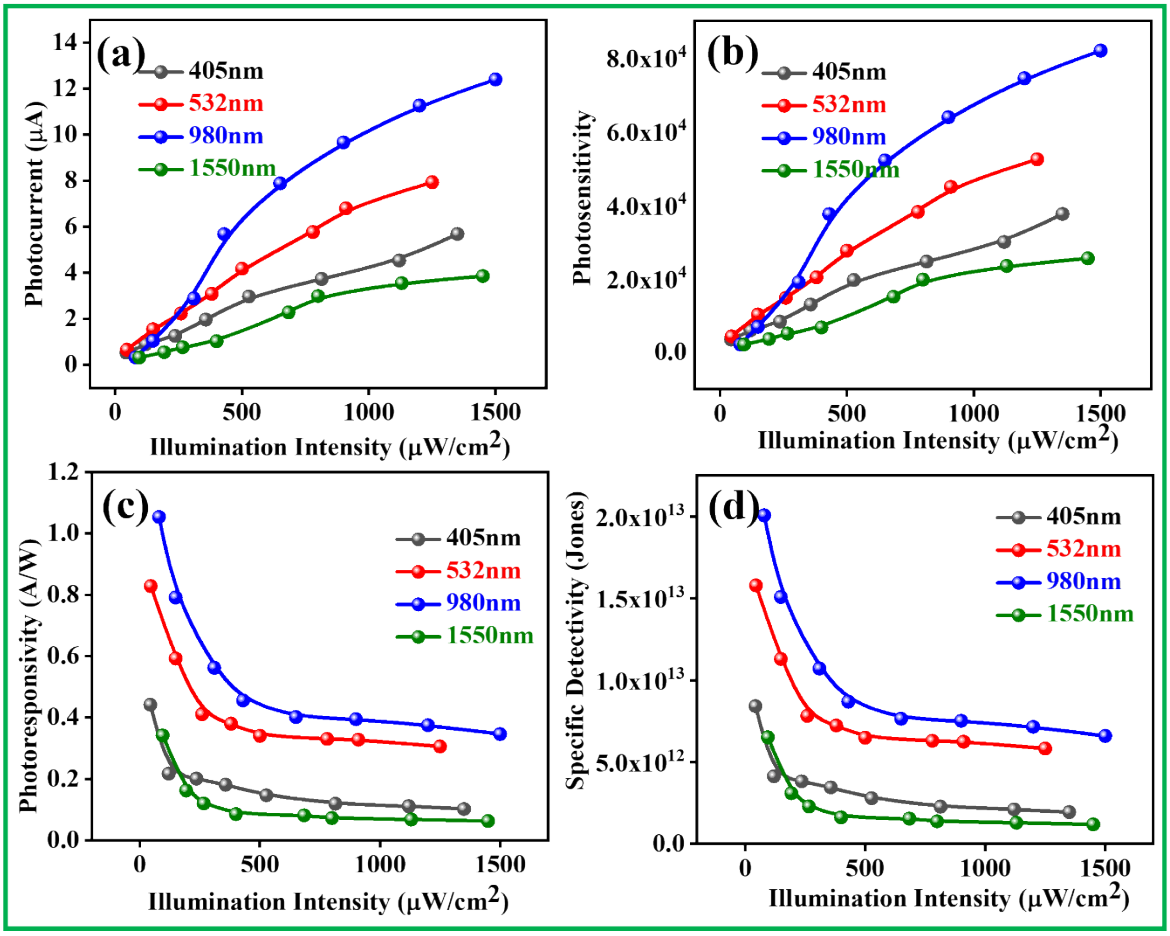

Figure S9. Performance of the photodetector ITO/ZnO/PbSe:$CsPbI_3$/CuSCN/P3HT/Au (device **B**). Photocurrent (**a**), photosensitivity (**b**), photoresponsivity (*R*) (**c**), and specific detectivity (D^*) (**d**) as functions of illumination intensity in self-driven mode under 405 nm, 532 nm, 980 nm, and 1550 nm illuminations.

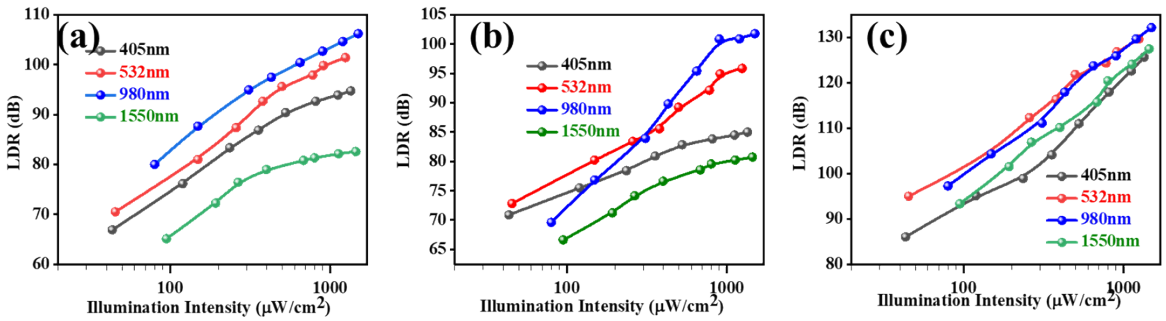

Figure S10. Illumination intensity dependent *LDR* for devices **A** (**a**), **B** (**b**), and **C** (**c**) under 405 nm, 532 nm, 980 nm, and 1550 nm illuminations, respectively.

Table S2. Important figure of merits to evaluate the performance of the p-n BHJ photodetector in self-driven mode under 405 nm, 532 nm, 980 m and 1550 nm illuminations, respectively.

Device Structure	Wavelength (nm)	Illumination Intensity μW/cm²	LDR (dB)	K	R (A/W)	D* (Jones)
Device A	405	43.5	70.88409	3.50×10^3	0.4417	8.42×10^{12}
	532	45.5	72.82279	4.37×10^3	0.82823	1.58×10^{13}
	980	80	66.62578	2.14×10^3	1.05325	2.01×10^{13}
	1550	95	66.62578	2.14×10^3	0.34172	6.51×10^{12}
Device B	405	43.5	66.88163	6.98×10^3	1.39743	2.53×10^{13}
	532	45.5	70.50307	2.37×10^3	2.14963	3.90×10^{13}
	980	80	79.97964	9.97×10^3	2.87891	5.22×10^{13}
	1550	95	65.08794	1.79×10^3	0.79577	1.44×10^{13}
Device C	405	43.5	86.00496	1.99×10^4	4.10534	1.40×10^{14}
	532	45.5	94.98491	5.61×10^4	7.31363	2.50×10^{14}
	980	80	97.21563	7.25×10^4	9.29034	3.17×10^{14}
	1550	95	93.30071	4.62×10^4	4.87296	1.66×10^{14}

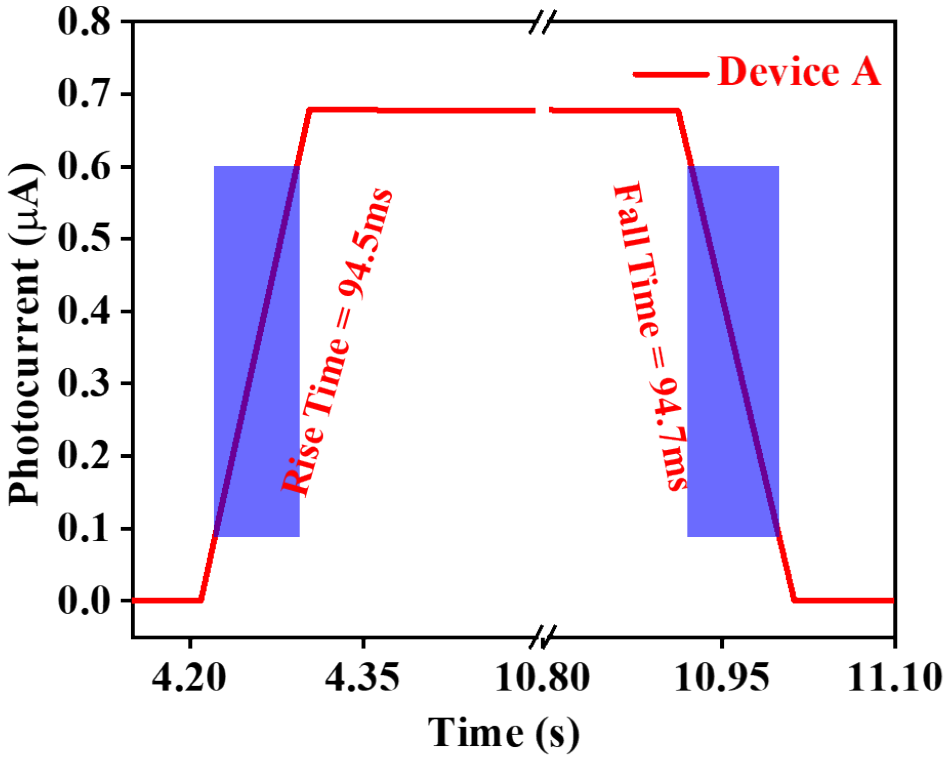

Figure S11. Measurement of the rising time (τ_r) and decaying time (τ_f) for photodetector ITO/ZnO/$CsPbI_3$/PbSe/CuSCN/P3HT/Au (device A) under 80 μW/cm^2 980 nm illumination at 0 V.

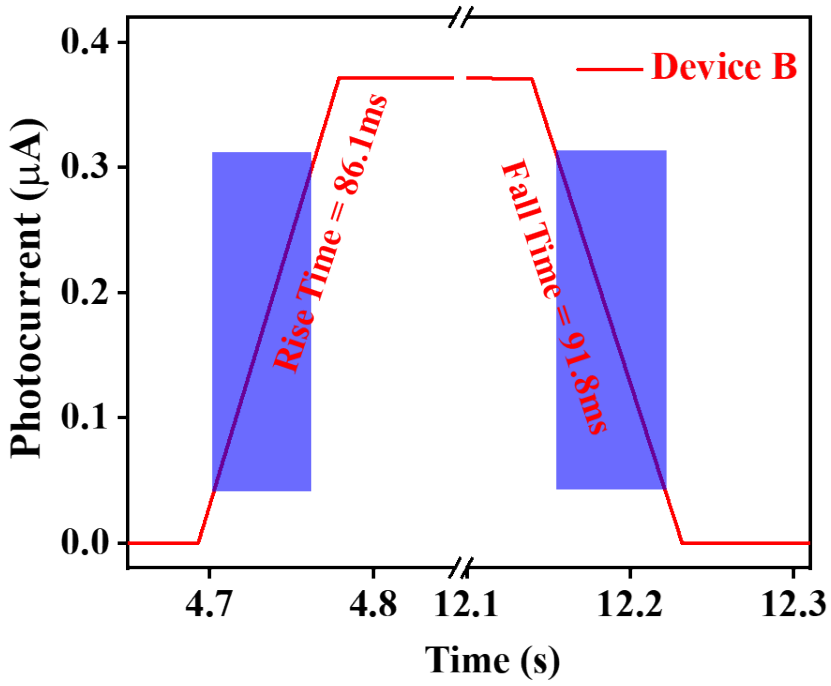

Figure S12. Measurement of the rising time (τ_r) and decaying time (τ_f) for photodetector ITO/ZnO/PbSe:$CsPbI_3$/CuSCN/P3HT/Au (device **B**) under 80 μW/cm^2 980 nm illumination at 0 V.

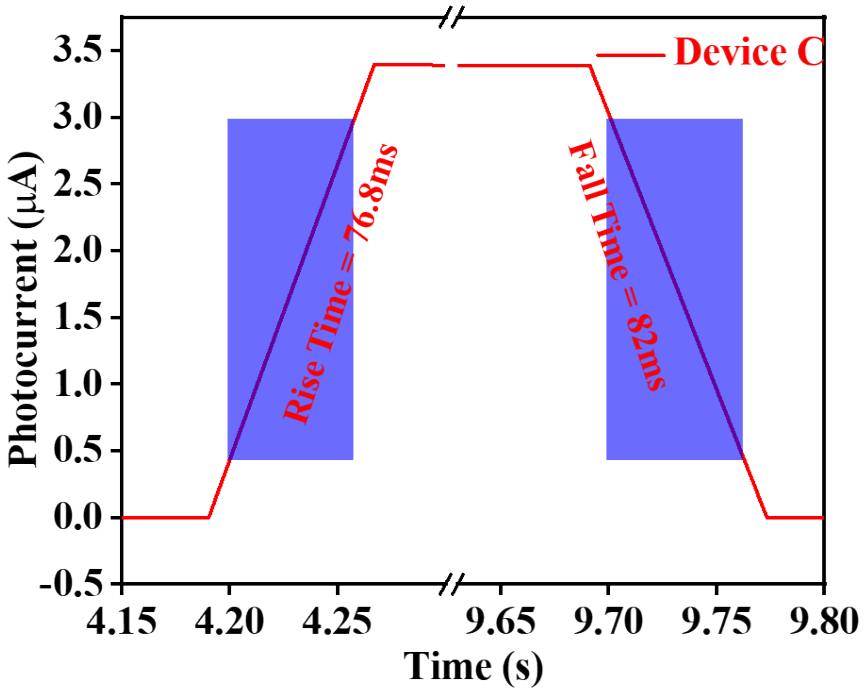

Figure S13. Measurement of the rising time (τ_r) and falling time (τ_f) for photodetector ITO/ZnO:Cs_2CO_3/PbSe:$CsPbI_3$/CuSCN/P3HT/Au (device **C**) under 80 μW/cm^2 980 nm illumination at 0 V.

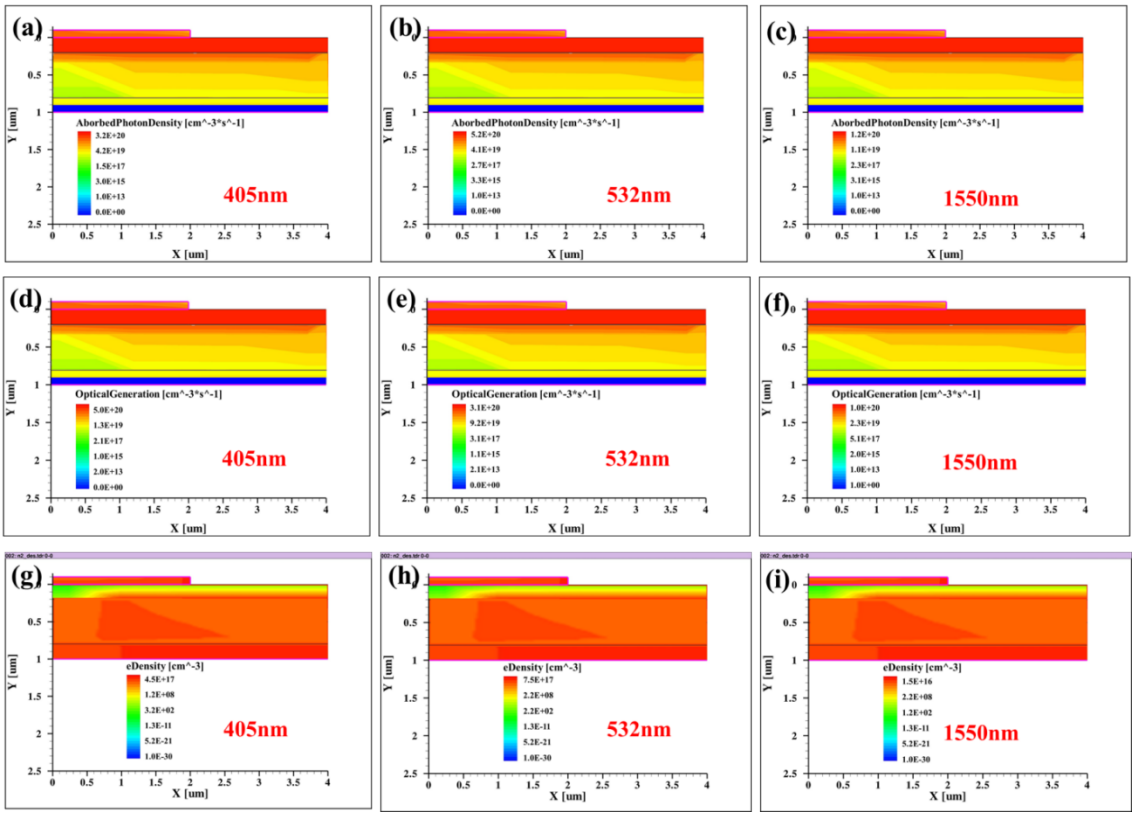

Figure S14. Simulated absorbed photon density (**a-c**), exciton generation (**d-f**) and electron mobilities (**g-i**) for device **C** under 405, 532, and 1550 nm illuminations.

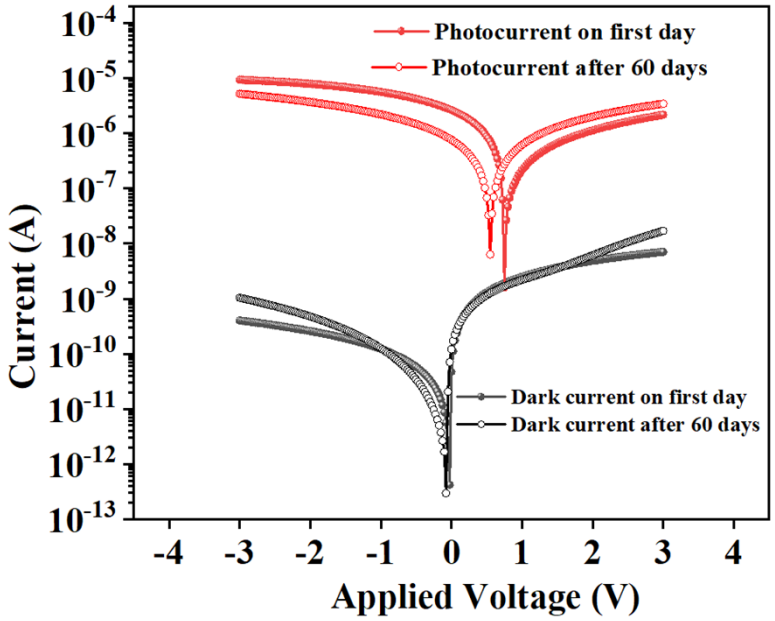

Figure S15. Stability assessment of Device C after 60 days, showing 3% reduced performance while maintaining self-powered behavior.

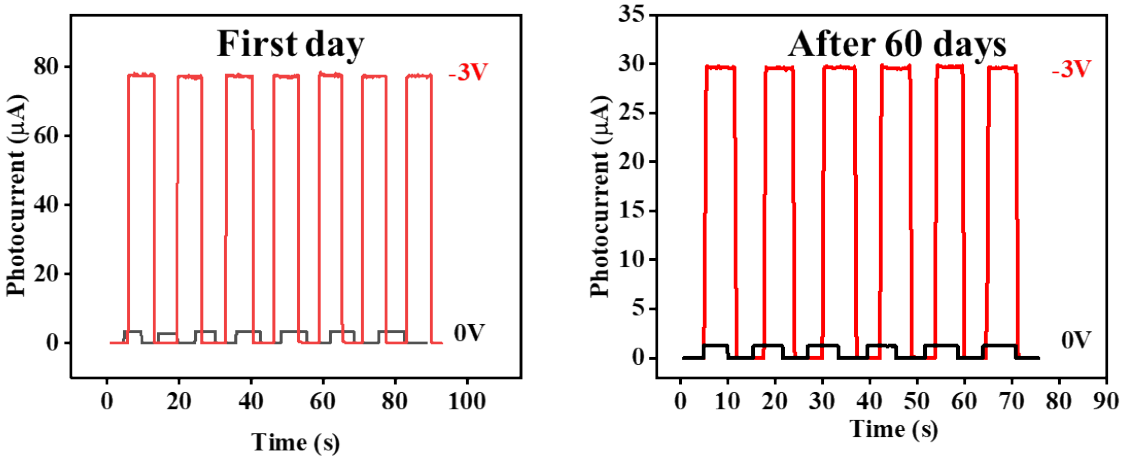

Figure S16. Time-dependent photodetector performance of Device C, demonstrating sustained self-powered behavior after 60 days.

Table S3. A comparison for device performances of the self-powered photodetectors based on perovskites and other nanomaterials.

Device Structure	Material used	Laser Wavelength	Illumination Intensity	*R* (A/W)	*D** (Jones)	ON/OFF ratio	Ref.
ITO/ZnO/PbSe/CsPbBr$_3$/P3HT/Au	PbSe, ZnO,CsPbBr3,P3HT	532nm	0.5 mWcm^{-2}	7.31	2.50× 10^{14}		**This**

ITO/ZnO:Cs_2CO_3/$CsPbI_3$:PbSe/CuSCN/Au	PbSe, ZnO,CsPbBr3,P3HT	980nm	0.5 $mWcm^{-2}$	9.29	3.17×10^{14}	2.06×10^{5}	**Work**
ITO/ZnO/PbSe:ZnO/ $CsPbBr_3$:P3HT/P3HT	PbSe, ZnO,CsPbBr3,P3HT	980nm	0.5 $mWcm^{-2}$	0.58	2.06×10^{14}	2.6×10^{5}	[1]
ITO/ZnO/PbSe:$CsPbBr_{1.5}I_{1.5}$/P3HT/Au	PbSe:$CsPbBr_{q.5}I_{1.5}$	405 nm	0.35$mWcm^{-2}$	4.41	4.27×10^{13}	2.73×10^{4}	[2]
		532 nm	0.5$mWcm^{-2}$	6.16	5.96×10^{13}	2.73×10^{4}	
		980nm	0.4$mWcm^{-2}$	4.46	4.31×10^{13}	4.95×10^{5}	
		1550nm	0.2$mWcm^{-2}$	3.87	3.74×10^{13}	1.01×10^{5}	
Gr/InSe/Au	InSe	200-400nm	--	0.365	1.26×10^{13}	--	[3]
ITO/BTO/Ag	ITO/BTO/Ag	405nm	111$mWcm^{-2}$	4.5×10^{-7}	3.00×10^{5}	--	[4]
Gr/PdSe/Gr	PdSe/Si	>1100nm	1.7 $mWcm^{-2}$	0.3	1.18×10^{13}	3×10^{5}	[5]
Au/$MAPbI_3$/Au	$MAPbI_3$	Sun light	0.01 $mWcm^{-2}$	0.61	1.5×10^{13}	--	[6]
Au/$CH_3NH_3PbI_3$/Au	$CH_3NH_3PbI_3$	375~808	0.01 × μWcm^{-2}	0.24	--	20	[7]
Pt/Al_2O_3/ZnO/FTO	Pt/Al_2O_3/ZnO	150 W Xe Lamp	50 $mWcm^{-2}$	0.644	2.96×10^{6}	--	[8]
$PtSe_2$/GaAs	$PtSe_2$/GaAs	650~808nm	0.11$mWcm^{-2}$	0.262	2.52×10^{12}	3×10^{4}	[9]
$PdSe_2$/$FA_{0.85}Cs_{0.15}PbI_3$	$PdSe_2$/$FA_{0.85}Cs_{0.15}PbI_3$	808nm		0.313	$\approx 10^{13}$	$\approx 10^{4}$	[10]
$PdSe_2$/Si	SiNW	0.2~0.6μm	27.5$nWcm^{-2}$	726	3.19×10^{14}	34.3	[11]

References

[1] M. Sulaman, S. Y. Yang, A. Imran, Z. Zhang, A. Bukhtiar, Z. Ge, Y. Song, F. Sun, Y. R. Jiang, L. Tang, B. S. Zou, Two Bulk-heterojunctions made of Blended Hybrid Nanocomposites for High-performance Broadband, Self-driven Photodetectors, *ACS Applied Materials & Interfaces*, 2023, 15, 25671–25683

[1] M. Sulaman, S. Y. Yang, A. Bukhtiar, P. Tang, Z. H. Zhang, Y. Song, A. Imran, Y. R. Jiang, Y. Cui, L. Tang, B. S. Zou, Hybrid Bulk-Heterojunction of Colloidal Quantum Dots and Mixed-Halide Perovskite Nanocrystals for High-Performance Self-Powered Broadband Photodetectors, *Advanced Functional Materials*, **2022**, 32, 2201527.

[2] M. Dai, H. Chen, F. Wang, M. Long, H. Shang, Y. Hu, W. Li, C. Ge, J. Zhang, T. Zhai, Y. Fu, P. A. Hu, Ultrafast and Sensitive Self-Powered Photodetector Featuring Self-Limited Depletion Region and Fully Depleted Channel with van der Waals Contacts, *ACS Nano*, **2020**, 14, 9098–9106.

[3] N. Ma, K. Zhang, Y. Yang, Photovoltaic–Pyroelectric Coupled Effect Induced Electricity for Self-Powered Photodetector System, *Advanced Materials*, **2017**, 29, 1703694.

[4] D. Wu, J. Guo, J. Du, C. Xia, L. H. Zeng, Y. Tian, Z. Shi, Y. Tian, X. J. Li, Y. H. Tsang, J. Jie, Highly Polarization-Sensitive, Broadband, Self-Powered Photodetector Based on Graphene/$PdSe_2$/Germanium Heterojunction, *ACS Nano*, **2019**, 13, 9907-9917

[5] R. Saraf, V. Maheshwari, Self-Powered Photodetector Based on Electric-Field-Induced Effects in MAPbI3 Perovskite with Improved Stability, *ACS Appl. Mater. Interfaces*, **2018**, 10, 21066–21072.

[6] J. Ding, H. Fang, Z. Lian, J. Li, Q. Lv, L. Wang, J. L. Sun, Q. Yan, A self-powered photodetector based on a CH3NH3PbI3 single crystal with asymmetric electrodes, CrystEngComm, **2016**, 18, 4405-4411.

[7] Z. Zhang, Q. Liao, Y. Yu, X. Wang, Y. Zhang, Enhanced photoresponse of ZnO nanorods-based self-powered photodetector by piezotronic interface engineering, *Nano Energy*, **2014**, 9, 237-244

[8] L. H. Zeng, S. H. Lin, Z. J. Li, Z. X. Zhang, T. F. Zhang, C. Xie, C. H. Mak, Y. Chai, S. P. Lau, L. B. Luo, Y. H. Tsang, Fast, Self-Driven, Air-Stable, and Broadband Photodetector Based on Vertically Aligned $PtSe_2$/GaAs Heterojunction, *Adv. Funct. Mater.* **2018**, 28, 1705970.

[9] L. H. Zeng, Q. M. Chen, Z. X. Zhang, D. Wu, H. Yuan, Y. Y. Li, W. Qarony, S. P. Lau, L. B. Luo, Y. H. Tsang, Multilayered $PdSe_2$/Perovskite Schottky Junction for Fast, Self-Powered, Polarization-Sensitive, Broadband Photodetectors, and Image Sensor Application, *Adv. Sci*. **2019**, 6, 1901134.

[10] D. Wu, C. Jia, F. Shi, L. H. Zeng, P. Lin, L. Dong, Z. Shi, Y. Tian, X. J. Li, J. S. Jie, Mixed-dimensional PdSe2/SiNWA heterostructure based photovoltaic detectors for self-driven, broadband photodetection, infrared imaging and humidity sensing, *J. Mater. Chem. A*, **2020**, 8, 3632-3642.